Supplementary Material

Radiation damage and dose limits in serial synchrotron crystallography
at cryo- and room temperatures

Eugenio de la Mora, Nicolas Coquelle, Charles S. Bury, Martin Rosenthal, James M. Holton, Ian Carmichael, Elspeth F. Garman, Manfred Burghammer, Jacques-Philippe Colletier, Martin Weik

- Supplementary Methods (Data reduction and processing; Refinement)
- Supplementary Introduction
- Supplementary Text S1 – Analysis of global (I/I_1) and specific (Cys127 – Cys6) radiation damage generated by a non-uniform beam represented by a three-beam model
- Supplementary Text S2 – Per-voxel simulation of global (I_n/I_1) and specific (Cys127 – Cys6) radiation damage
- Supplementary Tables S1 and S2
- Supplementary Figures S1 – S6
- Supplementary References

Supplementary Methods

Data reduction and processing

NanoPeakCell (NPC) (1) was modified to include a mode that allows for processing of SSRS data. In this mode, hit detection is only performed on the first frame after the shutter has fully opened. New parameters can be set in the input file. To turn on this mode, a ShootNTrap parameter has to be set to *True,* and the number of frames collected per sample position, as well as the number of frames to be considered as being empty because of shutter opening both need to be specified (e.g. *nperposition=100* and *nempty=5*, respectively). These modifications have been added to the version available on Github (github.com/coquellen/NanoPeakCell). Hit-finding parameters were adjusted upon visual inspection to determine background levels and a frame was considered to be a hit if at least five pixels were above threshold values of 5 and 10 counts for the low- and high-dose-rate series, respectively.

Selected hits were indexed and integrated with CrystFEL 0.6.2 (2). Indexing relied on *MOSFLM* (3), XDS (4) and Dirax (5). Datasets in the RT high- and low-dose rate series consisted of 19,818 and 20,182 indexed frames respectively, while the high-dose rate dataset collected at 100 K consisted of 9,051 indexed frames. Intensities were merged using Monte Carlo integration. Statistics of the first dataset of each series (RT-LDR, RT-HDR and CR1) are available in table S1, as well as the evolution of the principal serial-crystallography statistics ($I/\sigma(I)$, R_{split}, CC^*, multiplicity) as a function of dose for each series (Fig. S4).

In order to monitor the decrease in diffraction power as a function of dose, the intensities of all predicted reflections in each indexed diffraction pattern (I_n) of dataset *n* were summed. Briefly, integrated intensities with an $I/\sigma(I) > 0$ were extracted from the CrystFEL stream and normalized to the lowest-dose datasets, *i.e.* $I^{RT\text{-}LDR1}$, $I^{RT\text{-}HDR1}$, and I^{CR1} for the RT-LDR, RT-HDR and the cryo-series, respectively. Intensities from all predicted reflections on the detector were thus used, i.e. including those that extended beyond the resolution limit of the highest-dose data set in each series (2.04 and 1.9 Å for both RT series and the cryo series, respectively). Owing to the presence of ice rings in some of the diffraction patterns collected at 100 K, statistics in the resolution bins corresponding to ice rings were of mediocre initial quality. A custom-made python script was used to reject outliers based on abnormal background values of the integrated intensities. Briefly, all background values of the integrated intensities were extracted from the CrystFEL stream and split into 100 resolution bins (50 - 1.5 Å). The mean and standard deviation of background values ($\langle bkg \rangle$ and $\sigma(bkg)$, respectively) were then computed for each resolution bin. A resolution bin was considered suspect when the standard deviation $\sigma(bkg)$ was larger than the mean value $\langle bkg \rangle$. Once flagged, the threshold used for the detection of outlier intensities within an abnormal resolution shell was set to $2 * \sigma(bkg) + \langle bkg \rangle$, using average and standard deviation values from the closest regular resolution bin. For example, in the cryo1 CrystFEL stream, a total of 158,369 reflections were removed, corresponding to 7.42 % of the reflections within the flagged bins, or 1.96 % of all reflections in the dataset. The new CrystFEL stream was subsequently processed as described above. Upon rejection of these few reflections, the quality statistics considerably improved.

Refinement

PDB entry 2YBH was used as a starting model. Datasets corresponding to the lowest dose of the RT low-dose-rate series and the cryo series were first refined using rigid body refinement, then underwent simulated annealing to reduce model bias, after which the structures were refined by iterative cycles of real space refinement in *Coot* (6) and reciprocal space refinement in *Phenix* (7). Water molecules and solutes were added using *Phenix* and the final model was refined until statistical evaluators converged.

Supplementary Introduction

We evaluated two different models for reproducing the observed global (I_n/I_1 in Fig. 2 and 3a) and specific (integrated density in Fig. 4d) radiation damage under the highly non-uniform illumination used in this micro-beam study. We expect these models will be extensible to future studies with similarly small beams that may or may not have significant tails. The goal here is to deconvolute the effects of non-uniform illumination and extract the fundamental decay parameters that would have been observed with a perfectly uniform top-hat shaped beam. These parameters are the half-doses of global ($D_{1/2,g}$) and disulphide bond specific ($D_{1/2,s}$) damage. Using these parameters and perhaps a measured beam profile, the decay curves of this and future experiments may be predicted.

Non-uniform illumination, especially with significant tails such as employed here, present interesting challenges to dose calculation. Formally, dose (D) has units of absorbed energy per unit mass (J/kg), so that dose can be computed as the energy deposited into the sample by the X-ray beam divided by the mass of the sample. The problem arises when one considers that the tails of the beam may be regarded as having non-trivial intensity all the way out to infinity, irradiating a very large mass and therefore driving the formal dose to zero. This type of calculation is not very useful because the tails of the beam do not contribute as much to the data as the brighter core, and therefore the electron density observed as a result of the tails is that of a molecule that has endured far more than a zero dose.

This fact has led to more sophisticated ways of estimating the dose that is relevant to the image seen in the final electron density map. Many named weighted doses have now appeared in the literature (8), so for clarity we will delineate the definitions of "dose" used here. A convenient and popular metric computed by RADDOSE-3D (9) is the average dose to the region of the sample that has absorbed 95% of the total absorbed energy (AD_{95}). That is, a threshold is computed to define a volume containing 95% of the energy, and the ratio of Joules and kg within that volume are taken as a dose (AD_{95}). For Gaussian beams this is a well-behaved metric, and we shall define here AD_{G95} as the average dose computed for a Gaussian beam of specified widths. In the main manuscript, we refer to AD_{G95} simply as "average dose", calculated for example, with a Gaussian beam with full width at half maximum (FWHM) of 3.0 μm (horizontal, h) × 1.5 μm (vertical, v), yielding an average dose rate of 40.3 MGy/s.

However, the observed beam profile in our experiment was not strictly Gaussian: it had significant tails. Incorporating these tails in an AD_{95} calculation proved to be numerically unstable. For example, adding only 4% contribution of Lorentzian character to the tails reduced AD_{95} by a factor of ten. Adjusting the 95% criterion to be 96% changed AD_{95} by a factor of two. The reason for this is due to the problem of beam tails described above. The tails can change the mass of the 95% threshold significantly. Because a pure AD_{95} proved so sensitive to very small changes in the exact beam shape, its value as a metric is limited in this context. We therefore elected to use AD_{G95} instead. Using AD_{G95} instead of AD_{95} is essentially equivalent to neglecting the tails. That is, we define the volume of interest as that volume that would absorb 95% of the energy from a Gaussian beam, avoiding the explosion of the thresholded region inherent for Lorentzian beam tails. The energy deposited into this central region is almost identical for both beam shapes, so the AD_{G95} metric gives us a dose under the hottest and initially most influential part of the beam. This practice is recommended for future work.

The observed beam profile was explained well by a linear combination of Gaussian and Lorentzian beam shapes (eq. S12). This linear combination is often referred to as a pseudo-Voigt function. The Voigt function is defined as the convolution of a Gaussian and Lorentzian function (10), but the pseudo-Voigt is a convenient approximation to it. This approximation is accurate to within 5% near the peak and may deviate by as much as 20% in the tails, but here

it is not clear whether the observed beam shape was due to a convolution effect or an additive one. Both functions could be made to fit the observed beam shape reasonably well.

We define the fundamental dose D_{voxel} as the dose given to a very small volume under an arbitrary beam: a voxel. That is, a very small amount of energy is deposited in a similarly small mass, and that ratio is D_{voxel}. We expect the diffractive strength and chemical state of a voxel after D_{voxel} to be identical to that of a much larger region of crystal illuminated by a uniform, top-hat beam that delivered the same dose.

Both models presented below assume that the intensity decay is exponential with dose (D):

$$i = i_0 \, 2^{-\frac{D_{voxel}}{D_{1/2,g}}}$$

(eq. S1)

where $D_{1/2,g}$ is the dose at which the total Bragg-scattered intensity (i) from a uniformly-illuminated volume of crystal drops to half of its zero-dose value (i_0). Note that the more compact form of the exponential $2^x = \exp(\ln(2)*x)$ is convenient when using half-dose decay parameters. We further assume that the specific damage reaction involving the breaking of a disulphide bond also progresses exponentially, with the fraction of bonds still intact (f_{left}) in a uniformly-illuminated volume given by:

$$f_{left} = 2^{-\frac{D_{voxel}}{D_{1/2,s}}}$$

(eq. S2)

where $D_{1/2,s}$ is the dose at which half of the disulphide bonds are broken, and $f_0 = 1$.

A fundamental assumption of both models below is that the principle of linear superposition applies. For example, we assume that the total Bragg-scattered intensity from an unevenly-illuminated crystal is simply the sum of all its parts after breaking the crystal down into small enough volumes (c) so that each volume may be individually regarded as uniformly illuminated. This is a fundamental principle within RADDOSE-3D. Specifically:

$$I_n = \sum_c i_{c,n}$$

(eq. S3)

Where I_n is the total number of Bragg-scattered photons on image n, such as the observations shown in Fig. 3a, and $i_{c,n}$ is an instance of i in eq. S1: the Bragg intensity scattered from an evenly-illuminated volume (c) during the acquisition of image n.

We expect that linear superposition is a good approximation for total diffracted intensity, but it may or may not be so for specific damage. For completeness we shall explore this concern here. Consider the evolution of electron density as a disulphide bond breaks. If we collect one complete data set with negligibly small dose ($f_{left} \approx 1$) and another complete diffraction data set after all the disulphide bonds in the crystal are broken ($f_{left} = 0$) we will end up with two electron density maps: one is a 3D image of the molecule with an intact disulphide and the other fully broken. If we average these two maps we get an image that is a 50:50 superposition of the intact and broken molecules. This may be modelled with two alternate conformers at 50% occupancy each. If instead we average the diffraction data we also get an image that is very nearly that of a 50:50 mixture of intact and broken disulphides. Strictly speaking, averaging intensities ($\sim|\boldsymbol{F}|^2$) is not equivalent to averaging phased structure factors ($\boldsymbol{F}$), as there are cross-terms arising from averaging the square. However, in practice the resulting maps are visually quite similar. We therefore do not consider these intensity-average cross-terms to be a significant violation of the principle of linear superposition. What is a

concern is the possibility of intermediate states. Specifically: is the image of a 50:50 average of broken and unbroken states the same as the image of a half-broken molecule?

Consider for a moment the scenario where the bond breaks not by sudden rupture and popping instantaneously into a new position but rather that one sulphur atom moves slowly and linearly with dose (D_{voxel}) from its starting position in the intact bond to a final position in the fully broken state. In this case a dataset collected with all images at the half-dose ($D = D_{1/2,s}$) would reveal an electron density map containing the half-broken state: a sulphur atom located halfway between its starting and ending positions. This is not the same as a 50:50 average of the end points. This example is a simple case of an intermediate. However, if the bond rupture is indeed two-state we expect a dataset collected at $D_{voxel} = D_{1/2,s}$ to yield the same electron density map as a 50:50 mixture of data taken at $D_{voxel}=0$ and at $D_{voxel} >> D_{1/2,s}$. Put another way, a 50:50 average of data with $f_{left} = 1$ and $f_{left} = 0$ yields data with $f_{left} = 0.5$ for a two-state reaction. This linear superposition is a fundamental assumption of the present work. It is therefore important to point out that disulphide bond breakage does have an intermediate state (11, 12), but we shall regard the electron density changes observed here to be due to a two-state reaction. Indeed, because any experiment with dose contrast intrinsically averages data from regions of the sample that have experienced different doses, dose contrast can be regarded as an effective suppressor of information about intermediate states.

Another important example of linear superposition is the assignment of an experiment time (t) of 1 ms to image n=1, t=3 ms to image n=2, t=5 ms to image n=3, etc. This is because the photons on image n=1 arrived continuously between t=0 ms and t=2 ms. No doubt the distribution of arrival times was not flat, but as long as it may be regarded as linear the principle of superposition again applies. So, provided the consequences of radiation damage such as spot fading and bond breakage can be regarded as evolving linearly over the exposure time of a single image, the average result will faithfully represent the result at the average time. The average time for image 1 is t=1 ms. That is, we assume that the average of all diffraction patterns that would have been collected between 0 and 2 ms is the same as a diffraction pattern of the state of the crystal at t=1 ms.

The assumption of linear superposition allows us to calculate the apparent progression of the specific damage reaction observed in the electron density map (f_{map}) as expressed by a weighted sum of the reaction progression (f_{left}) in all the uniformly-illuminated volumes of the crystal:

$$f_{map} = \sum_{c} w_c f_{left,c} \qquad \text{(eq. S4)}$$

where w_c is the normalized weight assigned to volume c and $f_{left,c}$ is the true reaction progression within volume c. These weights arise from the intensity of illumination, the decay of diffraction, and other considerations outlined below, but in all cases the sum of all w_c is unity. Without the assumption of linear superposition there is no straightforward way to relate true damage progression f_{left} to the apparent progression f_{map}.

The extent of specific damage in this work was measured by integrating electron density. Integrated density is expected to have an arbitrary offset due to the unknown value of F000 and an arbitrary scale due to the unknown density overlap between the unreacted and damaged states. We therefore must modify f_{map} to put it on the same scale as the measurement, which was achieved here with simple linear regression:

$$WSD = a\, f_{map} + b \qquad \text{(eq. S5)}$$

where a is an arbitrary scale, b is an arbitrary offset, and WSD we define as the Weighted Specific Damage: the extent of damage progression that was observed.

We now describe our two models for defining and determining these weights. The first model "three-beam" was parametric: the crystal was divided into three independent regions, each with its own illuminating flux and dose rate. There were six fitted parameters overall: $D_{1/2,g}$ from eq. S1, $D_{1/2,s}$ from eq. S2, two per-volume beam weights (w_{hot}, w_{cold}) as in eq. S4, and the arbitrary scale (a) and offset (b) from eq. S5.

The second model "per-voxel" was more fine-grained: each voxel from a RADDOSE-3D run was treated as an independently decaying crystal in its own uniform beam and the resulting contributions summed. There were also six adjustable parameters: the weight of the beam tails ($h_{Lorentz}$), the crystal size (L_{xtal}), and then $D_{1/2,g}$, $D_{1/2,s}$, a and b as for the three-beam model. Overall fits to the data were comparable, with the "per-voxel" model being the most physically comprehensive but with much longer computational run times, and the "three-beam" model being the simplest and fastest to implement.

Supplementary Text S1 – Analysis of global (I/I_1) and specific (Cys127 – Cys6) radiation damage generated by a non-uniform beam represented by a three-beam model.

The decrease in diffraction power as a function of increasing dose (Fig. 2) cannot be fitted by a single exponential function. Thorne and co-workers have shown that the non-exponential decay of diffraction intensities at room temperature is a consequence of differential diffraction intensity decay due to the non-uniform irradiation provided by a Gaussian profile microbeam (13). In a *Gedankenexperiment*, Holton approximated non-uniform illumination using a two-beam model, in which the sample is irradiated by two beams differing by a factor of 10 in flux density. The apparent decay in diffraction power could be explained by two exponential functions with a tenfold difference between their rate constants (14). Here, we augment this concept to a three-beam model, to assess if our observed evolution of the specific damage could be explained by differential diffraction intensity decay due to the non-uniform irradiation.

We suppose exponential intensity decay (eq. S1) for two of the three beams, with contributions to the image proportional to their respective photon flux in photons/s. We constrain these two beams to have uniform illumination, as well as identical and disjoint footprint areas, making the dose rate under each beam proportional to flux. These two beams may be thought of as concentric areas: the core of the beam (hot beam; photon flux φ_{hot}) and a doughnut-shaped area around that core (cold beam; photon flux φ_{cold}). This allows the use of a single exponential decay parameter $D_{1/2,g}$. The dose rate under the cold beam is simply a modification of that under the hot beam, it is reduced by the ratio of the fluxes ($\varphi_{cold}/\varphi_{hot}$). The contribution of the third beam was proportional to its flux (φ_{const}), but otherwise invariant over the dose-range of this study. The overall intensity decay is described by the following equation:

$$\frac{I_n}{I_1} = \frac{\varphi_{hot}\, 2^{-\frac{AD_{G95}}{D_{1/2,g}}} + \varphi_{cold}\, 2^{-\left(\frac{AD_{G95}}{D_{1/2,g}}\frac{\varphi_{cold}}{\varphi_{hot}}\right)} + \varphi_{const}}{\varphi_{hot} + \varphi_{cold} + \varphi_{const}} \qquad \text{(eq. S6)}$$

where AD_{G95} is the average dose delivered by a Gaussian beam over the region of the crystal where 95% of the energy is deposited, as calculated RADDOSE-3D (9). This average dose was found to be much more numerically stable than the dose absorbed by the true (Voight-like) beam shape (see introduction above and eq. S12 below), and is simpler to calculate with RADDOSE-3D. In eq. S6, the third beam does not generate observable damage. This is consistent with a very broad and weak beam illuminating a very large area, such as a faint halo

of long tails. This third beam accounts for the plateau of residual intensity that remains even at very high values of average dose. Although there are three fluxes in S6, only two are free parameters because the denominator normalizes them.

For simplicity, let us now decompose eq. S6 and extract the Bragg intensity contribution arising from each beam:

$$i_{hot} = I_1 \frac{\varphi_{hot}}{\varphi_{total}} \, 2^{-\frac{AD_{G95}}{D_{1/2,g}}}$$

$$i_{cold} = I_1 \frac{\varphi_{cold}}{\varphi_{total}} \, 2^{-\left(\frac{AD_{G95}}{D_{1/2,g}} \frac{\varphi_{cold}}{\varphi_{hot}}\right)}$$

$$i_{const} = I_1 \frac{\varphi_{const}}{\varphi_{total}}$$

(eqs. S7)

Where I_1 is the total Bragg intensity observed on the first image and φ_{total} is the sum of all three fluxes (total flux). The diffraction decay weighted dose (DDWD), which takes into account the differential diffraction intensity decay (13), can then be computed as follows:

$$DDWD = AD_{G95} \, (i_{hot} + i_{cold} + i_{const})/I_1$$

(eq. S8)

To model the specific damage data, we have to consider that the overall intensity decay will be corrected by scaling during data processing, so that the sum of the different beam contributions will always be normalized to unity. The electron density difference map will therefore be a weighted sum of distinct structures illuminated by the two individual beams that contribute to the intensity decay. We can estimate the relative contribution, w_{hot} and w_{cold} of each beam as a function of the average dose AD_{G95}:

$$w_{hot} = \frac{i_{hot}}{i_{hot} + i_{cold}}$$

(eq. S9)

and

$$w_{cold} = \frac{i_{cold}}{i_{hot} + i_{cold}}$$

(eq. S10)

i_{const} is not taken into the normalization as it does not contribute to the decay of diffracted intensities and thus does not affect difference maps. To a first-order approximation, we consider that the specific-damage decay is exponential in each beam, with an exponential decay parameter $D_{1/2,s}$ (eq. S2) and that they can be linearly superimposed (eq. S4) to give a weighted specific damage metric, *WSD*.

$$WSD = a\left(w_{hot} \, 2^{-\frac{AD_{G95}}{D_{1/2,s}}} + w_{cold} \, 2^{-\frac{AD_{G95}}{D_{1/2,s}} \frac{\varphi_{cold}}{\varphi_{hot}}}\right) + \mathrm{b}$$

(eq. S11)

Two extra parameters were added to scale, *a*, and offset, *b*, this WSD function to the experimental data (eq. S5).

Estimation of parameters

The relative contributions of the hot and the cold beams are embodied in their ratio ϕ_{hot}/ϕ_{cold}, which was estimated by minimizing the difference between WSD and the specific damage experimental data.

For the RT series at 40.3 MGy/s, a final flux ratio of 25 between the hot and the cold beams was estimated, which corresponds to a contribution of 0.962 and 0.038 for the hot and cold beams, respectively. With this ratio, the exponential decay parameters are $D_{1/2,g}$ = 0.38 MGy (eq. S1) for global damage and $D_{1/2,s}$ = 0.08 MGy (eq. S2) for specific damage.

Supplementary Text S2 – Per-voxel simulation of global (I_n/I_1) and specific (Cys127 – Cys6) radiation damage

RADDOSE-3D (9) was used to calculate the dose rate at each point in the crystal and this distribution was subsequently used to compute the expected fading of each voxel with dose, as well as the apparent progression of specific radiation damage after accounting for this fading.

We postulated an X-ray beam with partial Lorentzian character which was represented by the sum of a Gaussian and a Lorentzian profile (pseudo-Voigt approximation):

$$d\varphi(x,y) = h_{Gauss}\,2^{-4\left(\left(\frac{x}{FWHM_x}\right)^2+\left(\frac{y}{FWHM_y}\right)^2\right)} + \frac{h_{Lorentz}}{1+4\left(\left(\frac{x}{FWHM_x}\right)^2+\left(\frac{y}{FWHM_y}\right)^2\right)} \quad \text{(eq. S12)}$$

where $d\varphi$ denotes the flux density at a given position and h_{Gauss} and $h_{Lorentz}$ are the relative contributions of the Gaussian and Lorentzian components of the beam. Both profiles were constrained to have the same horizontal (x) and vertical (y) full-width-at-half-maximum (FWHM) values of 3.0 μm (x) × 1.5 μm (y), but the Lorentzian component was weighted to account for 14% of the total flux. This X-ray intensity distribution was used to generate a 16-bit greyscale image of the beam profile in Portable Greymap (PGM) format which was provided to RADDOSE-3D. Each pixel represented a 0.2 × 0.2 μm^2 square patch of the beam profile and the entire PGM image ranged over a 200 × 200 μm^2 square.

The RADDOSE-3D run was conducted with 13.45 keV photons at a flux of 2.67×10^{12} photons/s and the crystal divided into 0.2 μm voxels. Tetragonal lysozyme from PDB ID 2ybh with 1.75 M Cl ions was specified with both photoelectron and fluorescent photon escape turned on. The rotation range was set to 0.01° to capture the beam divergence and the exposure time was set to 1 s so that the reported dose (Gy) was also a dose-rate (Gy/s).

The resulting per-voxel dose-rate and fluence (photons/area) values were averaged along the beam direction to yield a 2D map of dose (D_{voxel}) and relative illumination (w_{illum}) over the x-y plane. Voxels were then further weighted with a conical distribution:

$$w_{hit}(r) = \begin{cases} \dfrac{L_{xtal}-r}{r}, & r < L_{xtal} \\ 0, & r \geq L_{xtal} \end{cases} \quad \text{(eq. S13)}$$

This distribution was equal to unity at the centre of the beam, but fell off proportional to distance (r) from the beam centre out to the expected average edge dimension of the crystals

(L_{xtal}). w_{hit} was then made to be zero outside this radius. The purpose of this extra weight (w_{hit}) was to account for the random positioning of the beam on each crystal face. Over the serial data collection process some crystals might be hit at their exact centre, and others might be hit at their extreme corner. This has no impact on the contribution of voxels near the core of the beam, but parts of the crystal lattice far from the beam impact point will contribute less often to the total diffraction pattern. For example, when the main beam hits the centre of a square crystal with edge length L_{xtal}=15 μm all of the voxels at r=7 μm contribute to the data, but if the beam hits a corner of a square crystal there are only 1/4 as many voxels of diffracting material at this radius. The component of the beam with Lorentzian character means that these outlying parts of the crystal still experience a non-trivial number of photons, and indeed the residual long-exposure intensity observed in the diffraction data of the RT series at 40.3 MGy/s (triangles in Fig. 2) could not be reproduced with a Gaussian beam shape. Numerical integration revealed that the proper relative weighting of distant voxels was a conical distribution with base radius equal to the edge length of the cuboid crystal (eq. S13). The crystals used in the experiment were roughly 20 × 20 μm, but the effective average dimension L_{xtal} was made to be adjustable in the simulation. To expedite computation RADDOSE-3D was run once for a much larger cuboid crystal 60 × 60 μm and 20 μm thick, and then subsets of voxels were effectively selected via (eq. S13). The final best-fit simulation had L_{xtal}=15 μm.
After multiplying this "hit-rate weight" w_{hit} by the illumination level of each voxel (w_{illum}) from the RADDOSE-3D simulation, the fading due to radiation damage was applied. This fading factor (w_{fade}) was made to be exponential with voxel dose (D_{voxel}), reaching 0.5 at the half-dose for global radiation damage ($D_{1/2,g}$ = 0.4 MGy).

$$w_{fade}(D_{voxel}) = 2^{-\frac{D_{voxel}}{D_{1/2,g}}}$$

(eq. S14)

Note this D_{voxel} is a property of a single voxel, not an average property as in the three-beam model. The dose for each voxel (D_{voxel}) was computed by multiplying the dose rate obtained from RADDOSE-3D by the average exposure time of each image, which was 1 ms for the first image, 3 ms for the 2nd image, etc. The product of these three factors: illumination (w_{illum}), hit-rate (w_{hit}) and fading (w_{fade}) represented the relative contribution of each voxel to a given image. The sum of this combined weight over all voxels (w_{norm}) was taken to be proportional to the total Bragg intensity scattered into a given image:

$$w_{norm} = \sum_{voxels} w_{illum} w_{hit} w_{fade}$$

(eq. S15)

The ratio of w_{norm} obtained for each image to the value of w_{norm} for the first image is the per-voxel simulation-predicted I_n/I_1 shown in Fig. 3a.

Specific damage was also constrained to progress exponentially. The progression along this chemical reaction coordinate was represented by the fraction of un-reacted species (f_{left}), reaching 50% at the half-dose for specific damage ($D_{1/2,s}$ = 0.080 MGy) :

$$f_{left}(D_{voxel}) = 2^{-\frac{D_{voxel}}{D_{1/2,s}}}$$

(eq. S16)

This extent of the specific damage progression (f_{left}) was computed separately for each voxel using the same per-voxel dose (D_{voxel}) described above. The apparent progression of the

specific damage reaction in the electron density map (f_{map}) at each time point was taken to be the weighted sum of all f_{left} values:

$$f_{map} = \sum_{voxels} \frac{w_{illum} w_{hit} w_{fade} f_{left}}{w_{norm}} \qquad \text{(eq. S17)}$$

where w_{norm} is defined in eq. S14. This value of f_{map} was then scaled and offset (eq. S5) to align it with the observed integrated electron density values in Fig. 4d, just as it was with the three-beam model. These values were: a = 2.176, and b = -0.568 for the disulphide bridge Cys126-Cys7.

Estimation of parameters

RADDOSE-3D simulations were conducted on a grid of $D_{1/2,g}$ spaced every 0.1 MGy and $h_{Lorentz}$ spaced every 0.01. Numerical simulations of eq. S14 and eq. S15 were conducted on a grid of L_{xtal} spaced every 5 microns and $D_{1/2,s}$ spaced in 0.01 MGy. The optimal match to the observed general (I/I_1) and specific (integrated electron density) data was found at $D_{1/2,g}$ = 0.4 MGy, $D_{1/2,s}$ = 0.08 MGy, L_{xtal} = 15 μm and $h_{Lorentz}$ = 0.14.

Table S1. Data collection statistics for the lowest dose data sets in each series and refinement statistics for the first dataset in the RT low-dose rate and the cryo high-dose rate series. Values in brackets refer to the highest resolution shell. Doses are average value for 95% of the beam profile.

Data collection statistics			
Dataset	RT low-dose rate 1 RT-LDR1	RT high-dose rate 1 RT-HDR1	cryo high-dose rate 1 CR1
Temperature (K)	295	295	100
Dose rate (MGy/s)	2.4	40.3	40.3
Space group	$P4_32_12$	$P4_32_12$	$P4_32_12$
Unit cell parameters			
a (Å)	79.3	79.3	77.2
b (Å)	79.3	79.3	77.2
c (Å)	38.3	38.3	37.9
Indexed frames	20182	19818	9051
Observations	13066 (802)	17272 (870)	13066 (802)
Resolution (Å)	20.0–1.74 (1.77–1.74)	20.0–1.58 (1.60–1.58)	20.0–1.74 (1.77–1.74)
Rsplit (%)	13.54 (48.16)	9.71 (38.36)	6.82 (29.88)
CC* (%)	99.23 (92.43)	99.60 (93.80)	99.78 (94.5)
I/σI	6.50 (2.02)	8.44 (2.39)	11.45 (2.40)
Completeness (%)	100	100	100
Multiplicity	195.8 (106.9)	295.76 (123.8)	688.9 (266.2)

Refinement statistics			
PDB ID	6Q88		6Q8T
Resolution (Å)	20.00–1.74 (1.80–1.74)		20. 00–1.74 (1.80–1.74)
Number of reflections	13010 (1264)		12242 (1200)
Rwork (%)	18.16 (30.70)		19.81 (26.73)
Rfree (%)	20.38 (31.63)		24.59 (33.03)
Number of non-H atoms	1128		1149
Protein	1031		1018
Waters	89		114
Ligands	8		17
Number of residues	129		129
Average B-factor (Å^2)	27.55		23.07
Protein	26.54		22.24
Solvent	37.10		28.73
Ligands	51.71		34.61
r.m.s.d. bond lengths (Å)	0.005		0.010
r.m.s.d. angles (°)	0.77		1.11
Ramachandran favored (%)	98.43		99.21
Ramachandran allowed (%)	1.57		0.79
Ramachandran outliers (%)	–		–
Clash score	0.98		4.63

Table S2. $D_{1/2}$ values determined in this study under the different experimental conditions. $D_{1/2}$ values are obtained directly from the experimental I_n/I_1 curves (Fig. 2). $D_{1/2,g}$ corresponds to the half doses for global damage obtained by fitting the I_n/I_1 curves (Fig. 2) either according to the three-beam model (see Supplementary text S1 for details) or the per-voxel simulation (see Supplementary text S2 for details). $D_{1/2,s}$ corresponds to the half dose of specific damage to disulphide bonds obtained from the specific damage curves (Fig. 4) using the 3-beam model or the per-voxel simulation. N.A: not applicable.

		RT-LDR	RT-HDR	CR
$D_{1/2}$ (MGy)		0.36	0.57	15.3
$D_{1/2,g}$ (MGy)	3-beam model	0.34	0.38	17.8
	per-voxel	N.A	0.4	N.A
$D_{1/2,s}$ (MGy)	3-beam model	N.A	0.08	N.A
	Per-voxel	N.A	0.08	N.A

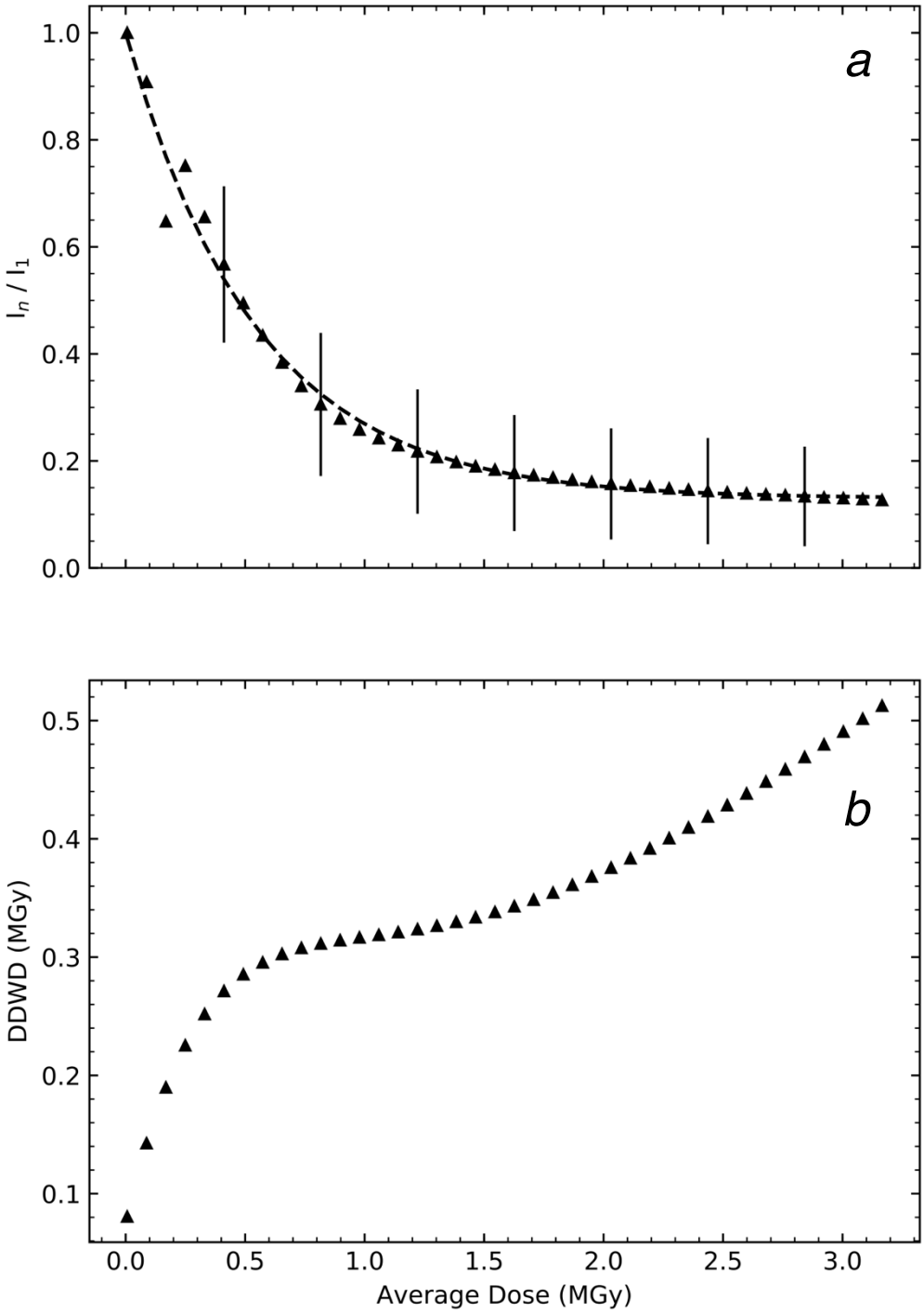

Figure S1: Decrease in diffraction power and diffraction decay weighted dose as a function of absorbed dose for the RT series at 40.3 MGy/s. (*a*) The sum of the intensities of all reflections up to the detector edges in all indexed diffraction patterns of a dataset, normalized to the sum of the first (*i.e.* lowest dose) data set (triangles, same data as in Fig. 2) is fitted (dashed line) according to Supplementary equation S6. Error bars correspond to the standard deviation of all sample positions in dataset *n*. (*b*) The diffraction decay weighted dose (DDWD) as a function of the average dose, computed according to Supplementary equation S8.

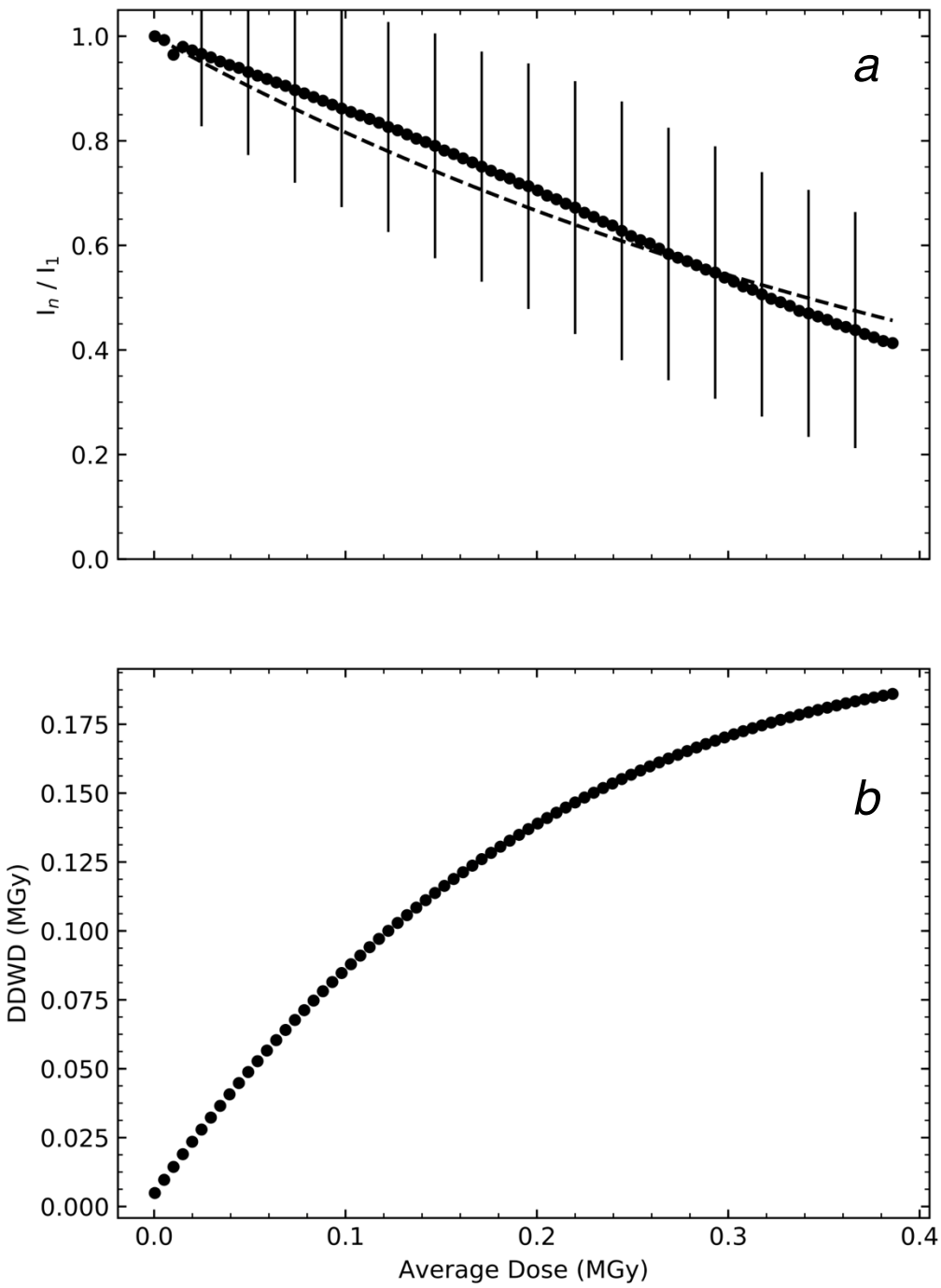

Figure S2: Decrease in diffraction power and diffraction decay weighted dose as a function of absorbed dose for the RT series at 2.4 MGy/s. (*a*) The sum of the intensities of all reflections up to the detector edges in all indexed diffraction patterns of a dataset, normalized to the sum of the first (*i.e.* lowest dose) data set (circles, same data as in Fig. 2) is fitted (dashed line) according to Supplementary equation S6. Error bars correspond to the standard deviation of all sample positions in dataset *n*. (*b*) The diffraction decay weighted dose (DDWD) as a function of the average dose, computed according to Supplementary equation S8.

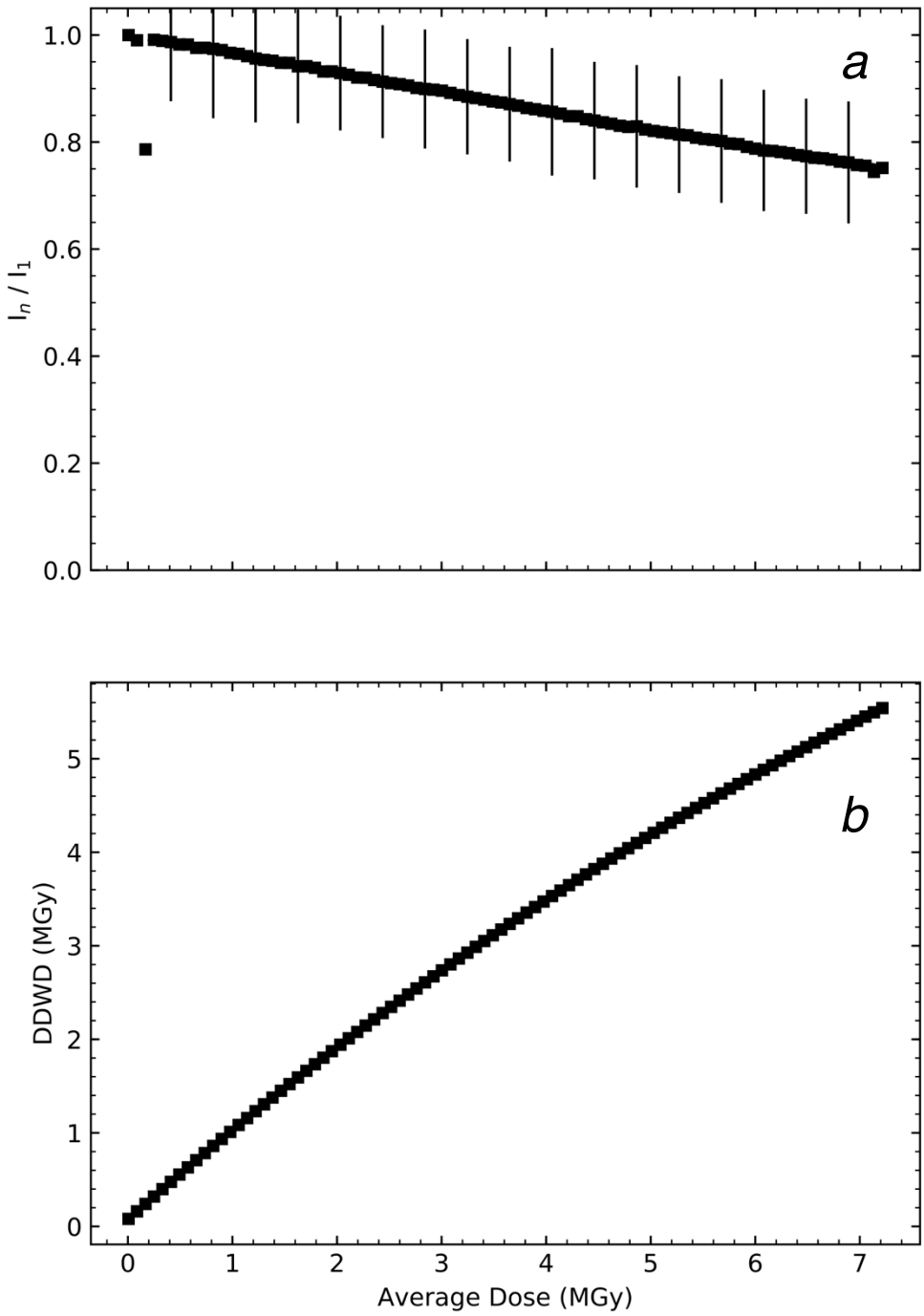

Figure S3: Decrease in diffraction power and diffraction decay weighted dose as a function of absorbed dose for the cryo series at 40.3 MGy/s. (*a*) The sum of the intensities of all reflections up to the detector edges in all indexed diffraction patterns of a dataset, normalized to the sum of the first (*i.e.* lowest dose) data set (squares, same data as in Fig. 2) is fitted (dashed line) according to Supplementary equation S6. Error bars correspond to the standard deviation of all sample positions in dataset *n*. (*b*) The diffraction decay weighted dose (DDWD) as a function of the average dose, computed according to Supplementary equation S8.

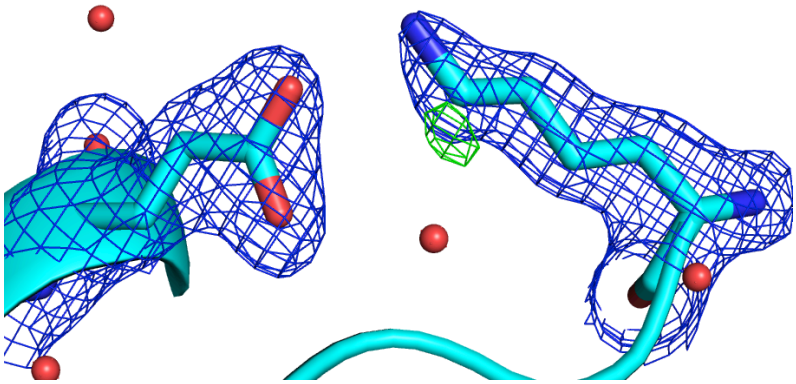

Figure S4: Glu7 at the protein surface is well ordered. $2F_o$-F_c (blue, 1 σ) and F_o-F_c (green, 3.5 σ, red, - 3.5 σ) maps of the lowest-dose dataset of the RT 2.4 MGy/s series (RT-LDR1; corresponding to an average dose (AD_{G95}) of 5 kGy). The model of RT-LDR1 (pdb code 6Q88) is superimposed.

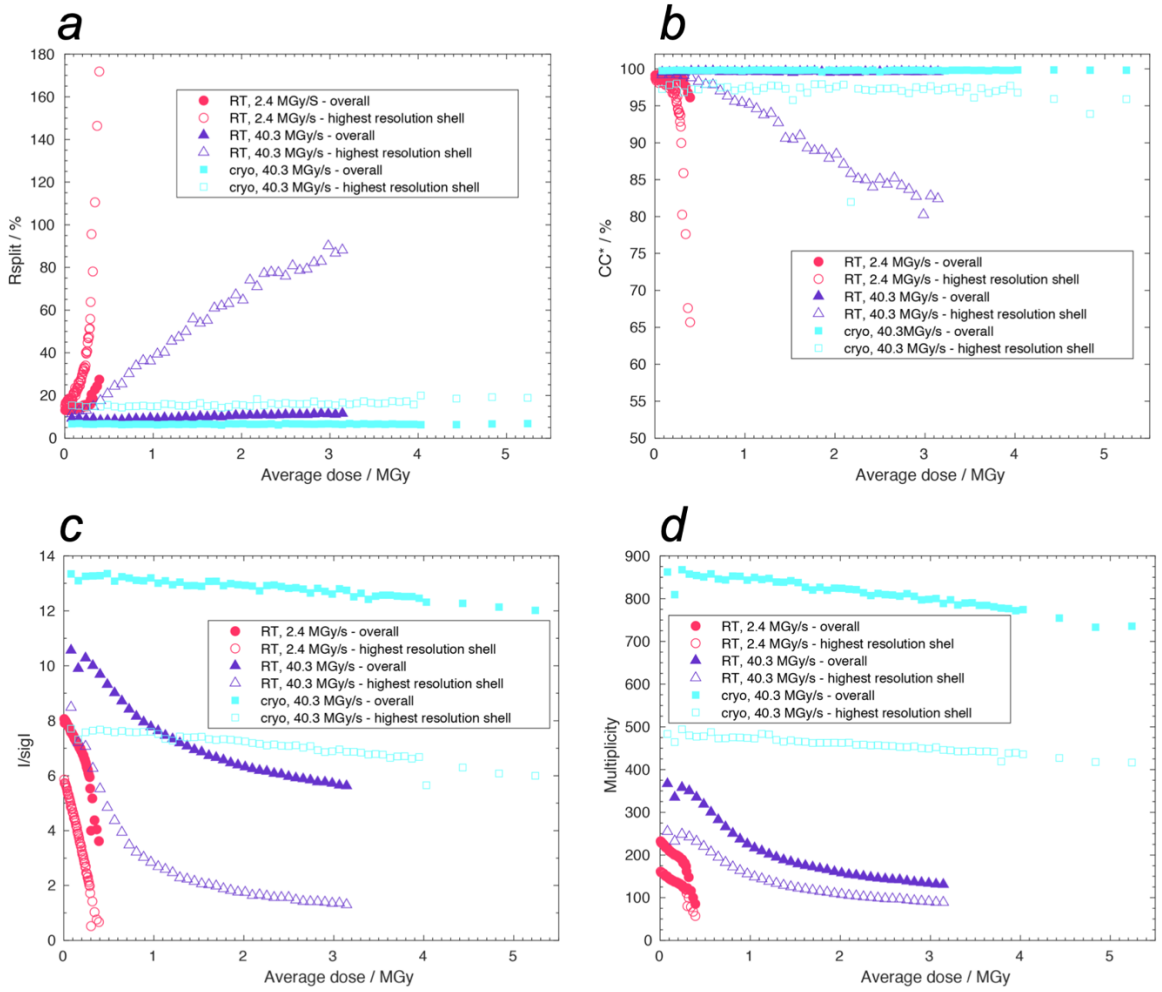

Figure S5: Evolution of the main statistical parameters (a) R_{split}, (b) *CC**, (c) $I/\sigma I$ and (d) multiplicity with increasing average dose (AD_{G95}) for the three different data series, RT low-dose series (red), RT high-dose series (purple) and 100 K high-dose series (cyan). For both RT series, the high-resolution shell is 2.10-2.04 Å, while for the 100 K series it corresponds to 1.97-1.92 Å.

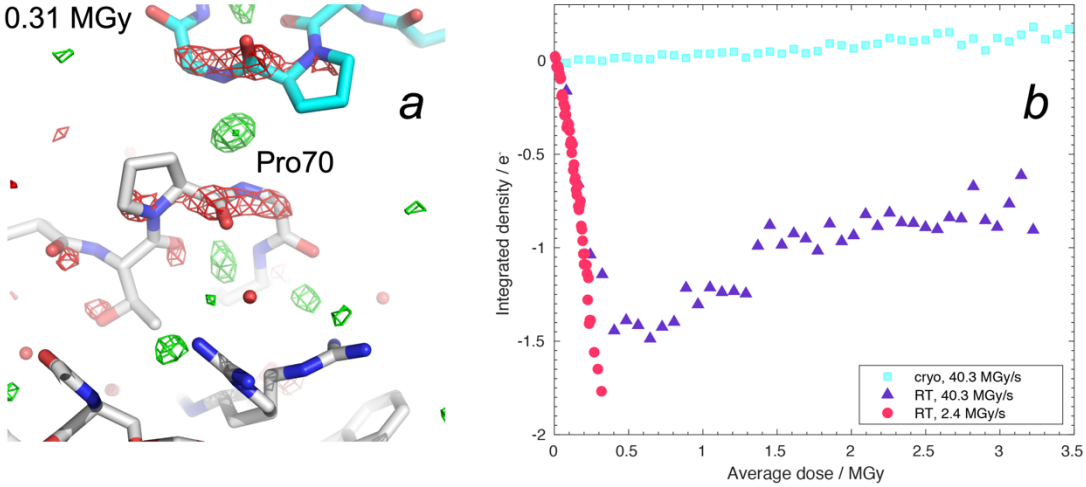

Figure S6: Radiation-induced changes at a proline residue as a function of increasing average dose. (*a*) Sequential difference Fourier map at Pro70 between the 64th (0.31 MGy) and the 1st data set in the RT 2.4 MGy/s series are shown at ±0.060 e$^-$/Å^3 (negative and positive peaks are in red and green, respectively). The model of the RT 2.4 MGy/s series dataset 1 (pdb code 6Q88) is superimposed on the difference Fourier map. Parts of two symmetry-related molecules are shown in grey and cyan. (*b*) Sum of integrated electron density in Fourier difference maps around each atom of Pro70 as a function of dose for the cryo and the two RT series. Note, only every 5th data point is shown at doses above 0.24 MGy for the RT 2.4 MGy/s series.

Supplementary References

1. N. Coquelle *et al.*, Raster-scanning serial protein crystallography using micro- and nano-focused synchrotron beams. *Acta Crystallographica Section D* **71**, 1184-1196 (2015).
2. T. A. White *et al.*, CrystFEL: a software suite for snapshot serial crystallography. *Journal of Applied Crystallography* **45**, 335-341 (2012).
3. H. R. Powell, O. Johnson, A. G. Leslie, Autoindexing diffraction images with iMosflm. *Acta crystallographica. Section D, Biological crystallography* **69**, 1195-1203 (2013).
4. W. Kabsch, Xds. *Acta Crystallographica Section D* **66**, 125-132 (2010).
5. A. Duisenberg, Indexing in single-crystal diffractometry with an obstinate list of reflections. *Journal of Applied Crystallography* **25**, 92-96 (1992).
6. P. Emsley, B. Lohkamp, W. G. Scott, K. Cowtan, Features and development of Coot. *Acta Crystallographica Section D* **66**, 486-501 (2010).
7. P. D. Adams *et al.*, PHENIX: a comprehensive Python-based system for macromolecular structure solution. *Acta Crystallographica Section D* **66**, 213-221 (2010).
8. E. F. Garman, M. Weik, X-ray radiation damage to biological samples: recent progress. *J Synchrotron Radiat* **26**, 907-911 (2019).
9. C. S. Bury, J. C. Brooks-Bartlett, S. P. Walsh, E. F. Garman, Estimate your dose: RADDOSE-3D. *Protein Science* **27**, 217-228 (2018).
10. B. H. Armstrong, Spectrum line profiles: The Voigt function. *Journal of Quantitative Spectroscopy and Radiative Transfer* **7**, 61-88 (1967).
11. K. A. Sutton *et al.*, Insights into the mechanism of X-ray-induced disulfide-bond cleavage in lysozyme crystals based on EPR, optical absorption and X-ray diffraction studies. *Acta crystallographica. Section D, Biological crystallography* **69**, 2381-2394 (2013).
12. M. Weik *et al.*, Evidence for the formation of disulfide radicals in protein crystals upon X-ray irradiation. *J Synchrotron Radiat* **9**, 342-346. (2002).
13. M. A. Warkentin, H. Atakisi, J. B. Hopkins, D. Walko, R. E. Thorne, Lifetimes and spatio-temporal response of protein crystals in intense X-ray microbeams. *IUCrJ* **4**, 785-794 (2017).
14. J. M. Holton, XANES measurements of the rate of radiation damage to selenomethionine side chains. *J Synchrotron Radiat.* **14**, 51-72. Epub 2006 Dec 2015. (2007).